

# Heterogeneous Iridium Single-Atom Molecular-like Catalysis for Epoxidation of Ethylene

Hongling Yang,<sup>○</sup> Xiaoxu Wang,<sup>○</sup> Qinggang Liu, Aijian Huang, Xun Zhang, Yi Yu, Zewen Zhuang, Ganggang Li, Yang Li, Qing Peng, Xin Chen,\* Hai Xiao, and Chen Chen\*



Cite This: *J. Am. Chem. Soc.* 2023, 145, 6658–6670



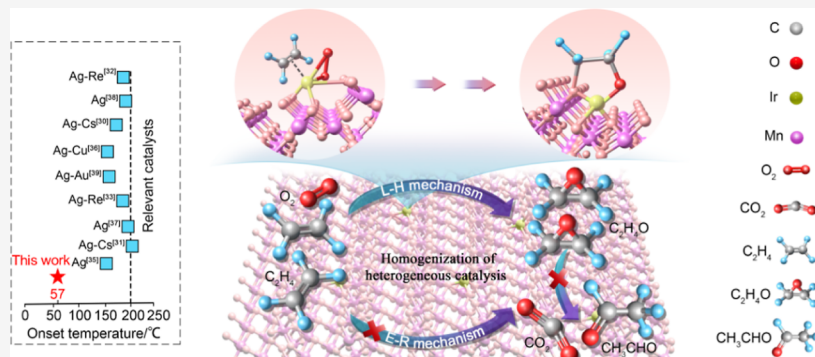
Read Online

ACCESS |

Metrics & More

Article Recommendations

Supporting Information



**ABSTRACT:** Developing efficient and simple catalysts to reveal the key scientific issues in the epoxidation of ethylene has been a long-standing goal for chemists, whereas a heterogenized molecular-like catalyst is desirable which combines the best aspects of homogeneous and heterogeneous catalysts. Single-atom catalysts can effectively mimic molecular catalysts on account of their well-defined atomic structures and coordination environments. Herein, we report a strategy for selective epoxidation of ethylene, which exploits a heterogeneous catalyst comprising iridium single atoms to interact with the reactant molecules that act analogously to ligands, resulting in molecular-like catalysis. This catalytic protocol features a near-unity selectivity (99%) to produce value-added ethylene oxide. We investigated the origin of the improvement of selectivity for ethylene oxide for this iridium single-atom catalyst and attributed the improvement to the  $\pi$ -coordination between the iridium metal center with a higher oxidation state and ethylene or molecular oxygen. The molecular oxygen adsorbed on the iridium single-atom site not only helps to strengthen the adsorption of ethylene molecule by iridium but also alters its electronic structure, allowing iridium to donate electrons into the double bond  $\pi^*$  orbitals of ethylene. This catalytic strategy facilitates the formation of five-membered oxametallacycle intermediates, leading to the exceptionally high selectivity for ethylene oxide. Our model of single-atom catalysts featuring remarkable molecular-like catalysis can be utilized as an effective strategy for inhibiting the overoxidation of the desired product. Implementing the concepts of homogeneous catalysis into heterogeneous catalysis would provide new perspectives for the design of new advanced catalysts.

## INTRODUCTION

Heterogeneous catalysts have been widely applied in industrial processes by virtue of their easy recyclability and operation, yet they often have complex structures, rendering it difficult to precisely design and regulate the catalytically active sites and their surrounding environments.<sup>1,2</sup> In contrast, homogeneous catalysts have intrinsic advantages on account of their defined coordination geometries, uniform active centers, and their coordination environments can be synthetically controlled with high precision, yet these catalysts face issues of recyclability and product separation.<sup>3,4</sup> In the past decades, various approaches have been employed to combine the advantages of homogeneous catalysis with those of heterogeneous catalysis, that is, implementing the mechanistic concepts of homogeneous catalysts into their heterogeneous counter-

parts.<sup>5–7</sup> In this regard, the most extensively developed strategy thus far is anchoring molecular metal complexes onto solid supports,<sup>8,9</sup> and the typical organometallic centers would be created near the surface, thereby conferring the reusability of the catalyst in various catalytic transformation processes. In addition, much progress has been made in catalyst recyclability and product separation after the nanocrystals are immobilized,<sup>10–13</sup> these approaches help us

Received: October 27, 2022

Published: February 21, 2023



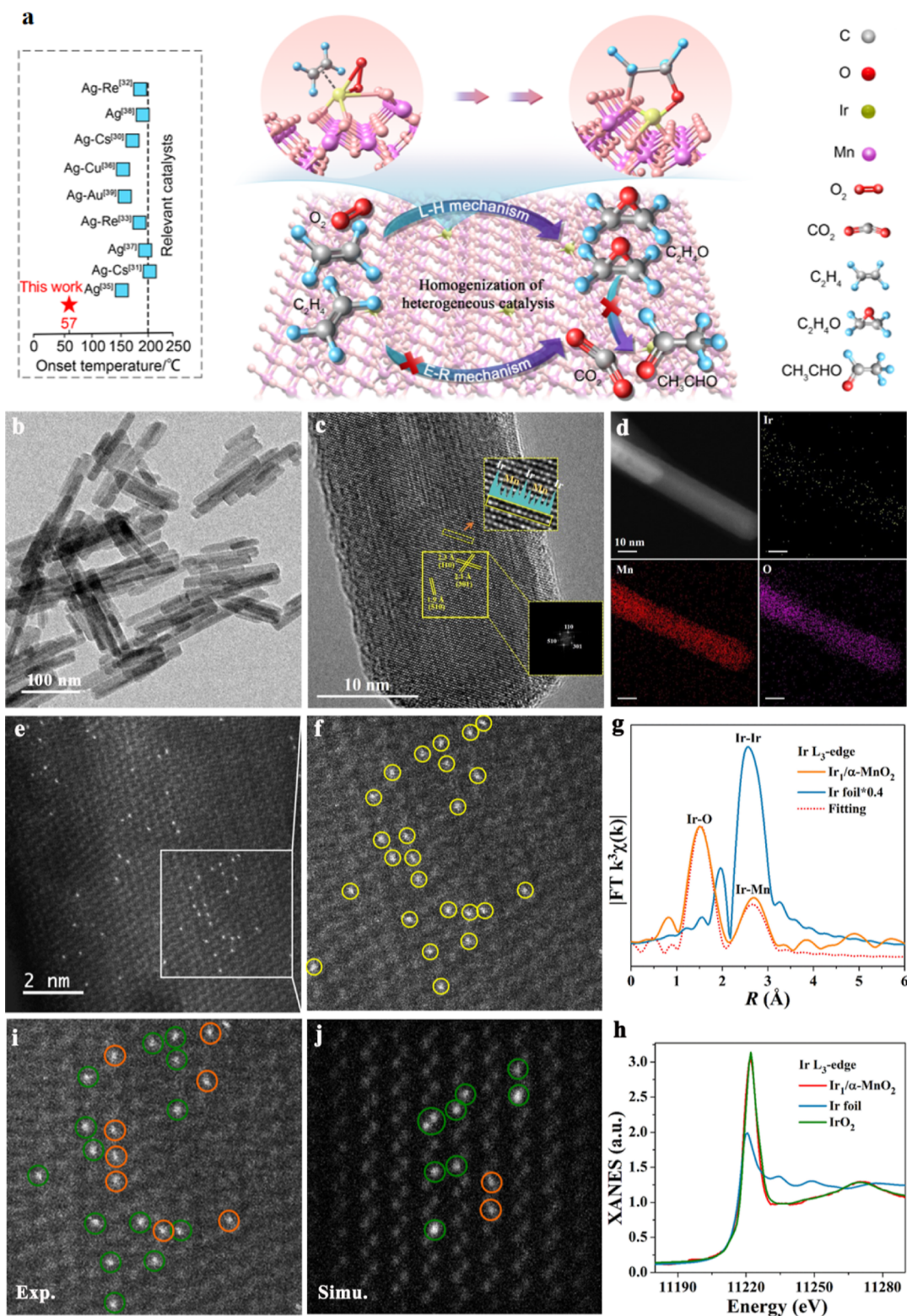


**Figure 1.** (a) Schematic illustration of the epoxidation of ethylene over  $\text{Ir}_1/\alpha\text{-MnO}_2$ . (b) TEM and (c) HRTEM images of  $\text{Ir}_1/\alpha\text{-MnO}_2$ . Insets in (c): (upper) intensity profile along the yellow zone (indicated by the orange arrow); (bottom) fast Fourier transform pattern of the selected area. (d) HRTEM image and corresponding elemental mapping results. (e,f) AC HAADF-STEM images of  $\text{Ir}_1/\alpha\text{-MnO}_2$ . (g) FT-EXAFS spectra of  $\text{Ir}_1/\alpha\text{-MnO}_2$  and Ir foil at the iridium  $\text{L}_3$ -edge. R, radial distribution function. (h) XANES of  $\text{Ir}_1/\alpha\text{-MnO}_2$ , Ir foil, and  $\text{IrO}_2$  at the iridium  $\text{L}_3$ -edge. (i,j) Magnified HAADF-STEM image of  $\text{Ir}_1/\alpha\text{-MnO}_2$  (i) and its corresponding simulated image (j) (green circles highlight the substitutional iridium sites, and orange circles represent the adsorbed iridium site).

understand the relationship between homogeneous and heterogeneous catalysis. However, much work remains to be done toward bridging these two catalysis research fields. Just

like the utilization of heterogeneous catalysts in the homogeneous catalytic reactions, exploiting homogeneous-like catalysts in the heterogeneous transformations not only

retains the high activity and selectivity but also reduces the amount of precious metals used.

Conceptually, catalysts that combine homogeneous and heterogeneous features are expected to be composed of defined active sites and insoluble in the reaction media during the reaction. The emerging single-atom catalysts (SACs) provide new opportunities to build a bridge between homogeneous and heterogeneous catalysis, which can be utilized to study the structure–activity relationship of various reactions at the molecular level, by virtue of their well-defined active structures and ease of mechanistic investigation.<sup>14–18</sup> Compared with conventional nanoparticle catalysts, SACs often demonstrate different chemistries and reaction pathways; these differences are because the metal sites in SACs often carry partially positive charges and thus influence their electronic densities, the interaction between metal and reaction species, and even the adsorption mode of the reaction intermediates.<sup>19–21</sup> When there is a unique coordination structure between the SACs and the reactant, it could be expected that the catalytic system would have a selectivity (almost) exclusively for a specific product.

Heterogeneous catalytic oxidation is an important class of reactions widely applied in industrial processes,<sup>22,23</sup> for example, in the selective oxidation of ethylene into the value-added ethylene oxide (EO),<sup>24–26</sup> yet despite decades of extensive investigations, the high selectivity is often achieved at the expense of catalytic activity. Achieving high selectivity with high activity is a great challenge because of the competing parasitic over-oxidation reaction. Silver is considered the most efficient catalyst in this regard and has been investigated intensively.<sup>27–29</sup> Thus far, the selectivity for EO can reach 90%, but only with the help of promoters (such as Cs,<sup>30,31</sup> Re,<sup>32,33</sup> C<sub>2</sub>H<sub>4</sub>Cl<sub>2</sub>,<sup>34,35</sup> Cu,<sup>36–38</sup> and Au<sup>39</sup>), and no consensus has been reached on the key catalytic mechanism of this reaction.<sup>40,41</sup> Besides, studies that comprehensively combine quantum-chemistry calculations and *in situ* spectroscopies on the reaction process of ethylene epoxidation are very scarce owing probably to the lack of a novel catalytic system that features both excellent performance and a well-defined structure.

Iridium is known to show unique characteristics in homogeneous organic reactions such as alkene or alkyne transformations, and iridium salts or complexes ( $[\{Ir(OH)\}-\text{cod}\}]_2$ ,  $[\{IrCl(\text{cod})\}]_2$ ,  $[\{Ir(\text{OMe})(\text{cod})\}]_2$ , and  $[\text{HIr}(\text{cod})-\text{(dppm)}]$  (cod = cyclooctadiene, dppm = Ph<sub>2</sub>PCH<sub>2</sub>PPh<sub>2</sub>)) catalyze these reactions mainly through forming  $\pi$ -alkene or  $\pi$ -alkyne species and thus obtaining the desired product selectively.<sup>42,43</sup> Considering that the chemical adsorption model of olefin on metal active centers is similar to the classic Dewar–Chat–Duncanson model of  $\pi$ -bonding in homogeneous metal–olefin complexes,<sup>44</sup> implementing this concept of homogeneous catalysis into the regime of heterogeneous catalysis to solve the problems in ethylene epoxidation may achieve effects that cannot be reached simply by heterogeneous catalysis.

In this work, we constructed a catalyst featuring iridium single-atom sites supported on  $\alpha$ -MnO<sub>2</sub> (Ir<sub>1</sub>/ $\alpha$ -MnO<sub>2</sub>) through a “redox and thermal diffusion” strategy, and the catalyst exhibited a remarkable activity in ethylene epoxidation, 7.6 times higher than that of Ag NPs/ $\alpha$ -Al<sub>2</sub>O<sub>3</sub>, with a near-unity selectivity (~99%) for the desired product EO. This excellent catalytic performance can be ascribed to the construction of a  $\pi$ -coordination structure between ethylene

and iridium single atoms, which promotes the formation of five-membered oxometallacycle intermediates and facilitates EO production. This unique  $\pi$ -coordination structure renders the mechanism of ethylene epoxidation here completely different from the E–R mechanism for conventional Ag-based catalysts, giving a lower reaction energy barrier and a smaller product desorption energy. Implementing homogeneous-like catalysts into the heterogeneous catalysis circumvents the bottleneck that the current silver-based catalysts face (for which the high selectivity is attained at the cost of activity), providing new perspectives for solving the central problems in ethylene epoxidation.

## ■ COMPUTATIONAL METHOD AND MODELS

To understand the synergistic effect, density functional theory (DFT) calculations were carried out *via* the Vienna ab initio simulation package (VASP) program by using projected augmented wave (PAW) potential<sup>45</sup> and the Perdew–Burke–Ernzerhof functional within the formulation of generalized gradient approximation.<sup>46</sup> The cutoff energy for the plane-wave expansion was set to 400 eV. The energy convergence criterion for the electronic self-consistent loop was set to  $10^{-5}$  eV, and the residual force on each atom was set smaller than 0.02 eV/Å for structural relaxations. We used the four-layer  $\alpha$ -MnO<sub>2</sub> (110) with a  $4 \times 4$  supercell to avoid the interaction between the replicas due to the periodic boundary conditions. A vacuum level of 15 Å was set to avoid interactions between periodic slabs. The reciprocal space was sampled by the gamma point in the Brillouin zone with a grid of  $1 \times 1 \times 1$ . The transition states were calculated *via* climbing image nudged elastic band methods. The harmonic frequency analysis of each optimized structure at the same level was carried out to verify that the stationary points exhibit no imaginary frequency, while the transition states exhibit one imaginary frequency.

The adsorption energies were calculated using the following equation

$$E_{\text{ad}} = E_{\text{ads}} - E_{\text{sub}} - E_{\text{m}}$$

where  $E_{\text{ads}}$  is the total energy of the substrate with the adsorbed ethylene molecule,  $E_{\text{sub}}$  is the energy of the substrate, and  $E_{\text{m}}$  is the energy of the reactant molecule in the gas phase. The desorption energies were calculated from the energy barrier of the adsorption process.

The method used for the minimum energy paths and related energies was the same PAW method of the same parameters with structure relaxations.

## ■ RESULTS AND DISCUSSION

**Synthesis and Structural Characterization of Ir<sub>1</sub>/ $\alpha$ -MnO<sub>2</sub>.**  $\alpha$ -MnO<sub>2</sub> nanorods were prepared through a one-pot hydrothermal method, and Ir<sub>1</sub>/ $\alpha$ -MnO<sub>2</sub> was synthesized *via* a thermal diffusion strategy (for the detailed experimental procedure, please see the *Supporting Information*). The schematic illustration of the epoxidation of ethylene over Ir<sub>1</sub>/ $\alpha$ -MnO<sub>2</sub> is demonstrated in Figure 1a. The powder X-ray diffraction pattern of Ir<sub>1</sub>/ $\alpha$ -MnO<sub>2</sub> matches well with the standard pattern of tetragonal cryptomelane (JCPDS 29-1020),<sup>47</sup> and there are no significant differences between the patterns of  $\alpha$ -MnO<sub>2</sub> and Ir<sub>1</sub>/ $\alpha$ -MnO<sub>2</sub> (Figure S1). The cryptomelane structure of Ir<sub>1</sub>/ $\alpha$ -MnO<sub>2</sub> was also verified *via* Raman spectroscopy (Figure S2). Nitrogen adsorption–desorption isotherms indicated that the Ir<sub>1</sub>/ $\alpha$ -MnO<sub>2</sub> nanorods

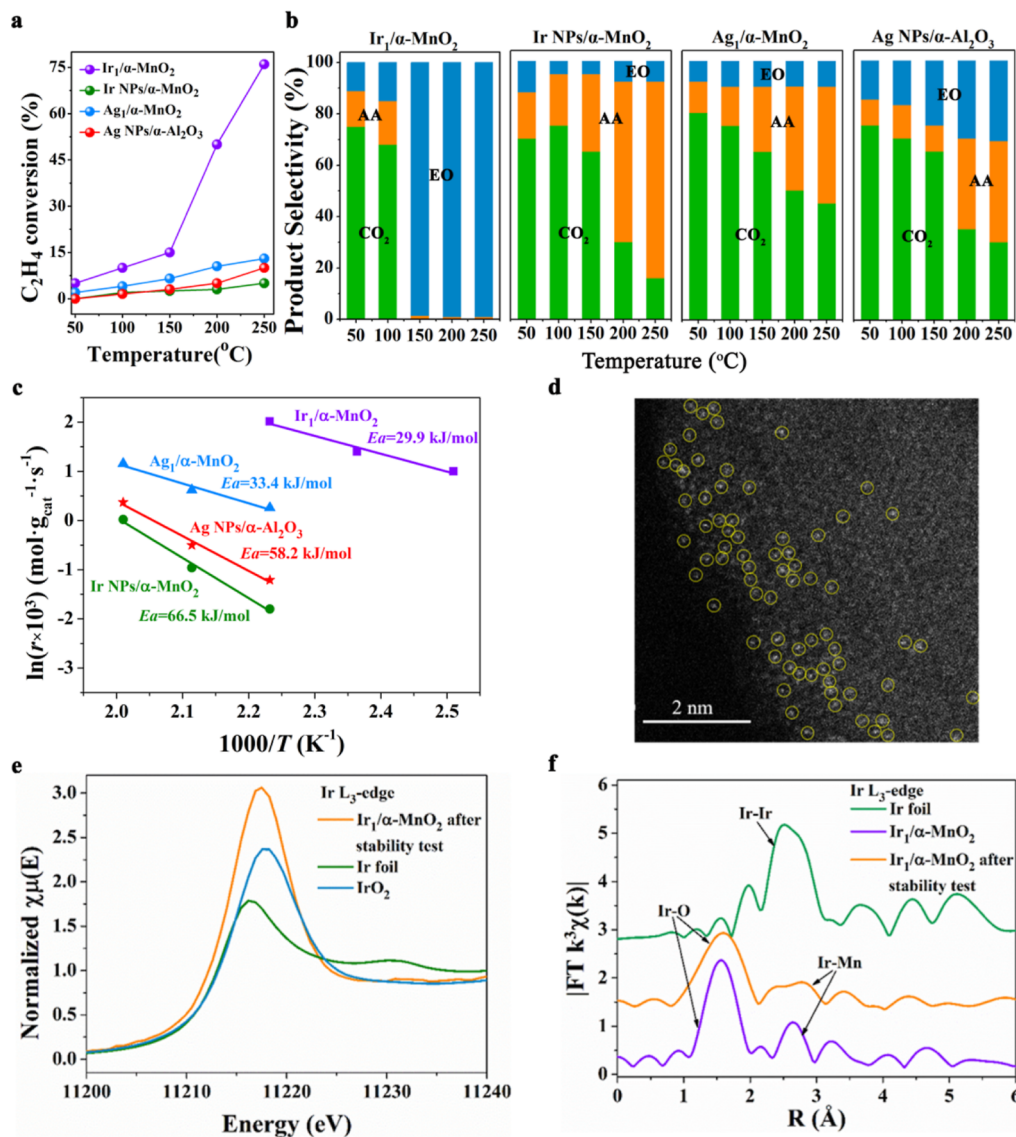


**Figure 2.** (a) Conversion of ethylene, (b) products' distribution, and (c) Arrhenius plots for ethylene epoxidation catalyzed by Ir<sub>1</sub>/α-MnO<sub>2</sub>, Ir NPs/α-MnO<sub>2</sub>, Ag<sub>1</sub>/α-MnO<sub>2</sub>, and Ag NPs/α-Al<sub>2</sub>O<sub>3</sub>. AA and EO stand for acetaldehyde and ethylene oxide, respectively. (d) AC HAADF-STEM image of the used Ir<sub>1</sub>/α-MnO<sub>2</sub>. (e) XANES of the used Ir<sub>1</sub>/α-MnO<sub>2</sub>, Ir foil, and IrO<sub>2</sub> at the iridium L<sub>3</sub>-edge. (f) FT-EXAFS spectra of fresh and used Ir<sub>1</sub>/α-MnO<sub>2</sub> and Ir foil.

have a high surface area of 72 m<sup>2</sup>·g<sup>-1</sup> (Figure S3). The iridium loading in Ir<sub>1</sub>/α-MnO<sub>2</sub> was determined to be 0.5 wt %, *via* inductively coupled plasma optical emission spectrometry. The high-resolution transmission electron microscopy (HRTEM) images (Figure 1b,c) show that Ir<sub>1</sub>/α-MnO<sub>2</sub> inherited the nanorod morphology (40–100 nm in length) of α-MnO<sub>2</sub>, with a uniform diameter of 10 nm. The corresponding energy-dispersive X-ray spectroscopy elemental mapping results (Figure 1d) show the elemental distribution of the Ir<sub>1</sub>/α-MnO<sub>2</sub> sample, in which iridium, manganese, and oxygen are uniformly distributed. In the aberration-corrected high-angle annular dark-field scanning transmission electron microscopy (AC-HAADF-STEM) images (Figure 1e,f), individual iridium atoms can be clearly observed as bright dots (highlighted by yellow circles).

The atomic dispersion of iridium was further confirmed by extended X-ray absorption fine structure (EXAFS) spectroscopy. The Fourier transforms of the iridium L<sub>3</sub>-edge EXAFS oscillations of the Ir<sub>1</sub>/α-MnO<sub>2</sub> (Figure 1g) reveal that the Ir-

Ir contribution at about 2.6 Å (typical for Ir foil) is absent for Ir<sub>1</sub>/α-MnO<sub>2</sub>, indicating that there are no iridium nanoparticles or clusters in Ir<sub>1</sub>/α-MnO<sub>2</sub>. Instead, a prominent peak at 1.6 Å corresponding to Ir–O scattering paths is observed. Note that the second and higher shell structures could be attributed to the bonding between Ir–Mn, which has a bond distance 0.1 Å longer than that of Ir–Ir. The least-squares FT-EXAFS fitting was used to determine the structural parameters for iridium in Ir<sub>1</sub>/α-MnO<sub>2</sub> (Figure S4), and the results show that each iridium single atom is coordinated with four oxygen atoms, with an average bond length of 2 Å (Table S1). The iridium L<sub>3</sub>-edge X-ray absorption near-edge structure (XANES) of Ir<sub>1</sub>/α-MnO<sub>2</sub> reveals a white-line peak position between those of the Ir foil and IrO<sub>2</sub> (Figure 1h), which mainly corresponds to the transition from occupied 2p to empty 5d states.<sup>48</sup> The oxidation state of iridium in Ir<sub>1</sub>/α-MnO<sub>2</sub> fitted from the XANES data is 3.52. X-ray photoelectron spectroscopy (XPS) was further conducted to analyze the valence state and electronic structure of the elements. The peak position of

iridium 4f for  $\text{Ir}_1/\alpha\text{-MnO}_2$  is located between those of  $\text{Ir}^0$  and  $\text{Ir}^{4+}$  (Figure S5). In addition, the introduction of iridium atoms onto  $\alpha\text{-MnO}_2$  was found to have altered the electronic structure of  $\alpha\text{-MnO}_2$ . As revealed by the manganese 3s XPS profile (Figure S6), the main peaks of manganese 3s in pristine  $\alpha\text{-MnO}_2$  are at 84.5 and 85.2 eV. In contrast, these two peaks shift, respectively, to 84.3 and 89.3 eV after the introduction of iridium single atoms, implying that the average oxidation state of manganese increases from 3.39 to 3.58, which is in accordance with the XANES results.

In the AC-HAADF-STEM images, the iridium atoms show higher contrast than the nearby Mn and O atoms because of the larger atomic number of iridium. The iridium single atoms may exist in two ways: by substituting the manganese atoms and by being adsorbed on the surface (i.e., at the interstitial sites). Based on the structure optimized *via* DFT, we conducted HAADF-STEM image simulation to investigate the location of iridium atoms (Figures S7 and S8), and the details of the simulation are summarized in the Supporting Information. We employed a model that includes both adsorbed iridium sites and substitutional iridium sites. The agreement between simulated results and experimental HAADF-STEM images (Figure 1g,i) clearly evidenced that iridium atoms exist by both substituting manganese atoms (highlighted with green circles) and being adsorbed on the catalyst surface (highlighted with orange circles).

**Catalytic Performance for Ethylene Epoxidation.** As silver-based catalysts have hitherto been regarded as the most active and selective materials for ethylene epoxidation,<sup>20</sup> we prepared Ag NPs/ $\alpha\text{-Al}_2\text{O}_3$  and Ag NPs/ $\alpha\text{-MnO}_2$  catalysts by a conventional impregnation method,<sup>29</sup> and the catalytic performances of these catalysts were found similar to those of other Ag-based catalysts reported in the literature.<sup>47,48</sup> We also prepared a Ag-based SAC denoted as  $\text{Ag}_1/\alpha\text{-MnO}_2$ , which exhibited different catalytic behaviors compared with its nanoparticle counterparts; an ethylene conversion of 15% and a selectivity of merely 10% for EO at 250 °C was found (Figure 2a,b). We further examined the catalytic performances of other  $\text{M}_1/\alpha\text{-MnO}_2$  SACs ( $\text{M} = \text{Ru, Rh, Pd, Ir, Pt, and Au}$ ) (Figure S9) and the effect of the flow rate of the reactant over the  $\text{Ir}_1/\alpha\text{-MnO}_2$  catalyst on ethylene conversion and EO selectivity and found that  $\text{Ir}_1/\alpha\text{-MnO}_2$  showed an ethylene conversion of 76% and a selectivity of 99% for EO at 250 °C, with the optimal flow rate of 50 mL·min<sup>-1</sup> (Figure S10). It can be observed that the distribution of reaction products [EO, acetaldehyde (AA),  $\text{CO}_2$ ] has changed drastically on  $\text{Ir}_1/\alpha\text{-MnO}_2$  compared with other catalysts (Figure 2b). The catalytic performance of  $\text{Ir}_1/\alpha\text{-MnO}_2$  surpassed those of our synthesized Ag NPs/ $\alpha\text{-Al}_2\text{O}_3$  and most previously reported catalysts (Table S2).

The orders of reaction with respect to ethylene and oxygen were 0.46 and 0.42, which were determined by monitoring the rate of ethylene consumption under various ethylene and oxygen partial pressures (Figure S11). The results of reaction orders were an indication that the reaction followed Langmuir–Hinshelwood (L–H) kinetics.<sup>50–54</sup> The influence of reactant partial pressures on catalytic performance is shown in Figure S12. It can be observed that both ethylene and oxygen partial pressures influence the catalytic activity. The conversion of ethylene increases with the increase of ethylene partial pressure and demonstrates saturation for higher pressures ( $P_{\text{C}_2\text{H}_4} = 0.15$  atm). Increasing oxygen partial

pressure can also increase the reaction activity, but the saturation effect at higher pressures is not as prominent. With the reactant pressure increasing from 0.01 to 0.15 atm, the EO selectivity remained almost constant (from 99.3 to 99.2%). The observed trends for increasing ethylene and oxygen feed pressures suggest that the selectivity for EO would not be significantly affected by increasing the total reactant pressures.

The thermocatalytic behavior of  $\text{Ir}_1/\alpha\text{-MnO}_2$  was found to be considerably different from its nanoparticle counterpart Ir NPs/ $\alpha\text{-MnO}_2$ . Ir NPs/ $\alpha\text{-MnO}_2$  gave a low ethylene conversion (<10%) and a negligible selectivity (<1%) for EO. These data indicate that the Ir SAC shows great advantages in the epoxidation of ethylene. The possible contribution of the  $\alpha\text{-MnO}_2$  support in  $\text{Ir}_1/\alpha\text{-MnO}_2$  for ethylene epoxidation was assessed by examining its activity separately under identical experimental conditions; an ethylene conversion of 5% was found, with EO being undetectable, which suggests that the  $\alpha\text{-MnO}_2$  support itself has some contribution to the overall ethylene oxidation activity, yet the selectivity for EO primarily originates from the atomically dispersed iridium species on  $\alpha\text{-MnO}_2$  and the interactions between them. These different catalytic performances are further reflected by their activation energies, with the effect of internal and external diffusion excluded (Figures S13 and S14). The apparent activation energy of  $\text{Ir}_1/\alpha\text{-MnO}_2$  is the lowest (29.9 kJ·mol<sup>-1</sup>) among all the investigated catalysts (Figure 2c), indicating that ethylene molecules could be activated much more readily over  $\text{Ir}_1/\alpha\text{-MnO}_2$ . Also, the significant difference in activation energy may result from the different reaction pathways on these catalysts. In addition, we investigated the catalytic performance of  $\text{Ir}_1/\alpha\text{-MnO}_2$  at a higher oxygen partial pressure and oxygen-to-ethylene ratio (3:2), and no AA or  $\text{CO}_2$  was detected in the reaction product at 250 °C.

Next, we conducted the catalytic stability test. As shown in Figure S15, after 24 h,  $\text{Ir}_1/\alpha\text{-MnO}_2$  showed good catalytic stability, with almost no decline in activity and EO selectivity. No iridium NPs were found in  $\text{Ir}_1/\alpha\text{-MnO}_2$  after the test, even under high-resolution HAADF-STEM (Figure 2d), and no diffraction peaks characteristic of metallic iridium were observed in the XRD pattern for the spent  $\text{Ir}_1/\alpha\text{-MnO}_2$  (Figure S16), further confirming the high dispersion of iridium single atoms after the ethylene epoxidation reaction. XANES shows that the iridium species remained oxidized on  $\text{Ir}_1/\alpha\text{-MnO}_2$  after the stability test (Figure 2e), and the results of extended XAFS reveal no detectable first- or second-shell Ir–Ir interactions, verifying the atomic dispersion of iridium (Figure 2f). In addition, the surface areas and pore volumes for the used  $\text{Ir}_1/\alpha\text{-MnO}_2$  were comparable to those of the freshly prepared  $\text{Ir}_1/\alpha\text{-MnO}_2$  (Figure S17 and Table S3), implying high stability after long-term tests. Raman spectroscopy was used to analyze whether there was carbon deposition on the used  $\text{Ir}_1/\alpha\text{-MnO}_2$  (Figure S18). No peaks characteristic of carbon species (~1328 cm<sup>-1</sup> corresponding to the vibration of C–H and ~1585 cm<sup>-1</sup> corresponding to the vibration of C=C) are observed in the Raman spectrum of the used  $\text{Ir}_1/\alpha\text{-MnO}_2$ ,<sup>55</sup> implying that there was almost no detectable carbon deposition on the catalyst surface during the test.

**Identification of the  $\pi$ -Coordination Structure between Iridium and Ethylene and the Nature of Oxygen Species.** We conducted *in situ* infrared (IR) absorption spectroscopy and *in situ* XPS to investigate the adsorption properties of the reactants on the  $\text{Ir}_1/\alpha\text{-MnO}_2$  surface and to track the structural evolution of iridium. The *in situ* IR study

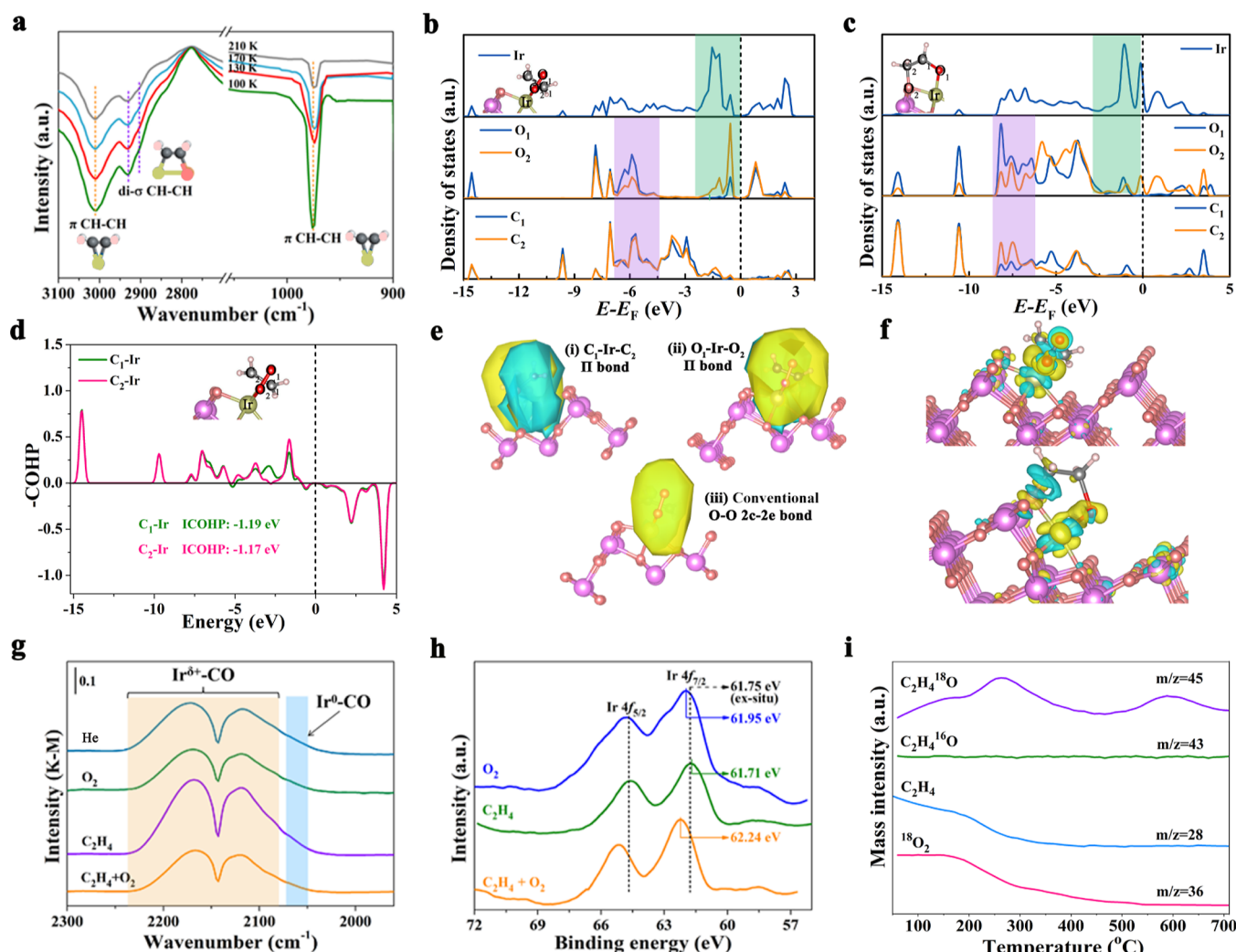


**Figure 3.** (a) *In situ* IR spectra of the adsorbates on  $\text{Ir}_1/\alpha\text{-MnO}_2$  at  $-173$ ,  $-143$ ,  $-103$ , and  $-63$   $^\circ\text{C}$ . (b,c) Calculated DOS of adsorbed  $\text{Ir}_1/\alpha\text{-MnO}_2$  with an aligned Fermi level. (d) COHP analysis for the interactions between carbon and iridium of  $\text{Ir}-\text{O}_2$ -ethylene. (e) SSAdNDP chemical bonding patterns for the (i)  $\text{C}_1\text{-Ir-C}_2$   $\pi$  bond, (ii)  $\text{O}_1\text{-Ir-O}_2$   $\pi$  bond, and (iii) conventional  $\text{O}-\text{O}$  2c-2e bond. (f) Calculated charge density distribution differences between adsorbed  $\alpha\text{-MnO}_2$ , oxygen, and ethylene; the yellow and cyan regions represent electron accumulation and depletion, respectively. (g) *In situ* IR spectra of CO adsorbed at full saturation coverage following varied pretreatment conditions measured at  $-173$   $^\circ\text{C}$ . (h) *In situ* XPS spectra of  $\text{Ir}_1/\alpha\text{-MnO}_2$  after the treatment of the sample with different gases at  $250$   $^\circ\text{C}$ ; dashed line: the location of the  $\text{Ir}$   $4f$  peak of  $\text{Ir}_1/\alpha\text{-MnO}_2$  at room temperature in ultrahigh vacuum; inset: peak value of  $\text{Ir}$   $4f_{7/2}$  after being treated by different gases. (i) TPRS of the reaction of ethylene with  $^{18}\text{O}_2$  over  $\text{Ir}_1/\alpha\text{-MnO}_2$ .

on the adsorption of reactants experiments was conducted at different temperatures by exposing the sample to a mixture of ethylene and oxygen.<sup>56</sup> Figure 3a shows the *in situ* IR spectra recorded after exposing the  $\text{Ir}_1/\alpha\text{-MnO}_2$  surface to ethylene at  $-173$   $^\circ\text{C}$ . The characteristic peaks due to the CH stretching mode of  $\pi$ -bonded ethylene were found at  $975$  and  $3009$   $\text{cm}^{-1}$ , and the peaks at  $2929$  and  $2901$   $\text{cm}^{-1}$  are assigned to the  $\text{CH}_2$  symmetric stretching mode of di- $\sigma$ -bonded ethylene.<sup>57</sup> The fact that the peaks at  $975$  and  $3009$   $\text{cm}^{-1}$  persist to  $-63$   $^\circ\text{C}$  indicates that the formation of  $\pi$ -bonded ethylene is stabilized in the presence of oxygen and iridium atoms on the catalyst surface. Notably, no peaks characteristic of ethylene were observed when sole ethylene was passed over the  $\text{Ir}_1/\alpha\text{-MnO}_2$  catalyst (Figure S19). Therefore, it can be inferred that the adsorption of ethylene is greatly promoted in the atmosphere comprising both ethylene and oxygen. The oxygen on the  $\text{Ir}_1/\alpha\text{-MnO}_2$  surface can stabilize  $\pi$ -bonded ethylene,<sup>57</sup> which can be further confirmed by DFT calculations (*vide infra*). The

occupied  $\pi$ -orbital of ethylene donates an electron to an empty metal iridium orbital, and the empty ethylene  $\pi^*$ -orbital accepts an electron from the occupied metal iridium orbitals;<sup>58</sup> these interactions promote the adsorption of ethylene on the surface. The heterogeneous iridium single atoms anchored on  $\alpha\text{-MnO}_2$  nanorods interact with ethylene and molecular oxygen (acting as ligand analogues), and the resulting iridium–oxygen–ethylene complex on the  $\alpha\text{-MnO}_2$  support is supposed to be one of the most nearly uniform supported metal complex catalysts, that is, “molecular-like catalysts” (Figure S20).

By contrast, the spectra of the adsorbates on Ir NPs/ $\alpha\text{-MnO}_2$  under similar conditions merely show peaks at  $2901$  and  $2883$   $\text{cm}^{-1}$  (Figure S21), which are assigned to di- $\sigma$ -bonded ethylene. The peak intensities of di- $\sigma$ -bonded ethylene remain approximately constant at  $-173$ ,  $-143$ , and  $-103$   $^\circ\text{C}$ . For the  $\text{Ag NPs}/\alpha\text{-Al}_2\text{O}_3$  catalyst, the peak at  $2895$   $\text{cm}^{-1}$  (assigned to di- $\sigma$ -bonded ethylene) is observed, and this peak disappears at

–63 °C (Figure S22). As both Ir NPs/ $\alpha$ -MnO<sub>2</sub> and Ag NPs/ $\alpha$ -Al<sub>2</sub>O<sub>3</sub> catalysts exhibit low activities for ethylene epoxidation, it can be inferred that the epoxidation of ethylene on Ir<sub>1</sub>/ $\alpha$ -MnO<sub>2</sub> proceeds predominantly through  $\pi$ -bonded ethylene, and the di- $\sigma$ -bonded ethylene is a spectator species not essential to ethylene epoxidation. Also, the predominant reaction pathways on the Ir NPs/ $\alpha$ -MnO<sub>2</sub> and Ag NPs/ $\alpha$ -Al<sub>2</sub>O<sub>3</sub> are different from that on Ir<sub>1</sub>/ $\alpha$ -MnO<sub>2</sub>, as evidenced by the IR data, in which merely di- $\sigma$ -bonded ethylene was captured on the catalyst's surface. Moreover, the presence of  $\pi$ -bonded ethylene on the iridium single atom could modify the structure of Ir<sub>1</sub>/ $\alpha$ -MnO<sub>2</sub> during ethylene epoxidation<sup>59</sup> and thereby alter its adsorption ability of reactants.

The established simulation model was further investigated in terms of density of states (DOS),<sup>60</sup> crystal orbital Hamiltonian populations (COHP),<sup>61</sup> solid-state adaptive natural density partitioning (SSAdNDP),<sup>62</sup> and charge density difference calculation.<sup>63</sup> The many overlapping states between Ir $^{\delta+}$ , O<sup>2–</sup>, and C below the Fermi level indicate the hybridization between iridium, oxygen, and carbon orbitals (Figure 3b,c), which reflects the bond formation and the strong interaction between iridium, oxygen, and ethylene. Specifically, for the initial step involving the adsorption of molecular oxygen and ethylene on an iridium single-atom site, the two carbons (C<sub>1</sub> and C<sub>2</sub>) in the ethylene molecule show similar DOS, suggesting that the interactions between the two carbons and iridium are almost identical. The COHP was further calculated to obtain the bonding and antibonding information of the electron densities, which was performed using the LOBSTER code.<sup>64</sup> As shown in Figure 3d, the C–Ir covalent interaction consists completely of bonding states at all energy levels below the Fermi energy, whereas all the states are antibonding above the Fermi energy, implying that this structure is stable. Moreover, C<sub>1</sub>–Ir and C<sub>2</sub>–Ir demonstrate similar COHP diagrams. The integrated value of COHP (ICOHP) of C<sub>1</sub>–Ir and C<sub>2</sub>–Ir bonds in Ir–O<sub>2</sub>–C<sub>2</sub>H<sub>4</sub> are –1.19 and –1.17 eV, respectively. The above results demonstrate that the C<sub>1</sub>–Ir and C<sub>2</sub>–Ir bonds in the Ir–O<sub>2</sub>–C<sub>2</sub>H<sub>4</sub> are similar, indicating that the two carbon atoms in ethylene have similar interactions with iridium, further confirming the interaction between iridium and ethylene in the form of  $\pi$ -coordination. In addition, for the DOS of the second step in the entire reaction process, we can see that there is also a notable DOS change of the oxygen (O<sub>2</sub>) in manganese oxide, which helps to form the five-membered oxametallacycle intermediates, confirming the essential role of the  $\alpha$ -MnO<sub>2</sub> support.

To further explore the unique chemical bonding in this catalytic system, we utilized the SSAdNDP program for postprocessing the VASP calculation results,<sup>65</sup> the SSAdNDP projection algorithm was applied here to represent the delocalized plane-wave DFT results on a localized atomic orbital basis.<sup>62</sup> The SSAdNDP analysis identifies the delocalized ( $nc$ -2e bonds,  $n > 2$ ) bonding elements in the catalytically active center. According to our calculations, one unit cell of the Ir–O<sub>2</sub>–ethylene system contains two 3c–2e bonds, including a C<sub>1</sub>–Ir–C<sub>2</sub>  $\pi$  bond and an O<sub>1</sub>–Ir–O<sub>2</sub>  $\pi$  bond (Figure 3e(i,ii)), with the occupation number 1.9–2.0 lel. It is worth noting that the O<sub>1</sub>–Ir–O<sub>2</sub>  $\pi$  bond almost overlaps with the conventional O–O 2c–2e bond (Figure 3e(iii)), which is consistent with the *in situ* IR results. In combination with the COHP analysis, the interaction between Ir and adsorbed C/O is dominated by d- $\pi$  orbital bonding. Thus, this combination of bonds enhances the stability of Ir–O<sub>2</sub>–ethylene

and promises unique catalytic performance. Charge density difference results show that the strong interaction between iridium, oxygen, and ethylene molecules comes from not only Ir–O  $\sigma$ -bonding but also the back-donation from the iridium toward the antibonding  $\pi^*$  orbital of ethylene (Figure 3f). Next, we used carbon monoxide as a probe to obtain the accessible surface sites on the catalyst under realistic reaction conditions. The Ir<sub>1</sub>/ $\alpha$ -MnO<sub>2</sub> sample was treated with different gases (He, O<sub>2</sub>, ethylene, mixed reaction gas of ethylene, and O<sub>2</sub>) at 250 °C, followed by exposure to CO at –173 °C. The residual CO molecules and physically adsorbed species on the catalyst surface were removed under vacuum. It can be observed that, in any case, two bands in the range of 2230–2080 cm<sup>–1</sup> were found (Figure 3g), which can be ascribed to the symmetric and antisymmetric vibration modes of Ir $^{\delta+}$ –CO complexes.<sup>66</sup> Also, no bands characteristic of the adsorption of CO on Ir<sup>0</sup> (2080–2050 cm<sup>–1</sup>) (Figure S23) were detected. These results suggest that iridium remained in the form of single atoms under realistic reaction conditions.

The adsorption properties of the reactants were also investigated by *in situ* XPS, which was carried out after the pretreatment of Ir<sub>1</sub>/ $\alpha$ -MnO<sub>2</sub> with different gases at 250 °C in an *in situ* reaction cell attached to the end station of XPS. The electronic properties of metal on the catalyst surface changed when the catalyst surface was treated with different gases, which revealed information on the interaction between reactants and catalysts.<sup>67</sup> As shown in Figure 3h, when the sample was exposed to O<sub>2</sub> at 250 °C, the binding energy of iridium 4f for Ir<sub>1</sub>/ $\alpha$ -MnO<sub>2</sub> shifted to higher energy by 0.2 eV compared with that with no exposure to any gas (the position of the dotted line). This is because when the sample was exposed to O<sub>2</sub>, the electron was transferred from iridium to oxygen. By contrast, there was only a small difference (less than 0.1 eV) in the binding energies of iridium 4f after Ir<sub>1</sub>/ $\alpha$ -MnO<sub>2</sub> was treated with ethylene. This indicates that when the sample was treated with ethylene, there was barely any electron transfer under reducing conditions, suggesting that the interaction between iridium single atoms and ethylene was far weaker than that between iridium and O<sub>2</sub>. Moreover, in the mixed-gas atmosphere (ethylene + O<sub>2</sub>), the binding energy of iridium 4f shifted by 0.5 eV with respect to that without any gas treatment, and the shift in binding energy was even larger than that in the O<sub>2</sub> atmosphere. In general, when a reducing gas, ethylene, is added to O<sub>2</sub>, the binding energy of iridium single atoms is expected to decrease, but in our catalytic system here, the binding energy of iridium 4f becomes higher, and this indicates that the electrons of iridium single atoms are transferred to the  $\pi$  bond of ethylene during the epoxidation of ethylene because iridium SAC interacts with ethylene and oxygen to form a molecular-like catalyst. Also, the interaction between iridium single atoms and the reactants was strengthened when the sample was exposed to the mixed gas compared with that treated by any single gas, thus facilitating the epoxidation of ethylene. In contrast, there was almost no discernible shift of iridium 4f binding energy for Ir NPs/ $\alpha$ -MnO<sub>2</sub> (Figure S24), implying that its electronic structure was barely altered under such reaction conditions. These *in situ* XPS results were well consistent with the IR adsorption data.

For an oxidation reaction, the nature of the oxygen species on the catalyst surface is of great significance and can be revealed through temperature-programmed reaction spectroscopy (TPRS) in the reaction of ethylene with isotopic oxygen (<sup>18</sup>O<sub>2</sub>) on the Ir<sub>1</sub>/ $\alpha$ -MnO<sub>2</sub> surface (Figure 3i). The TPRS

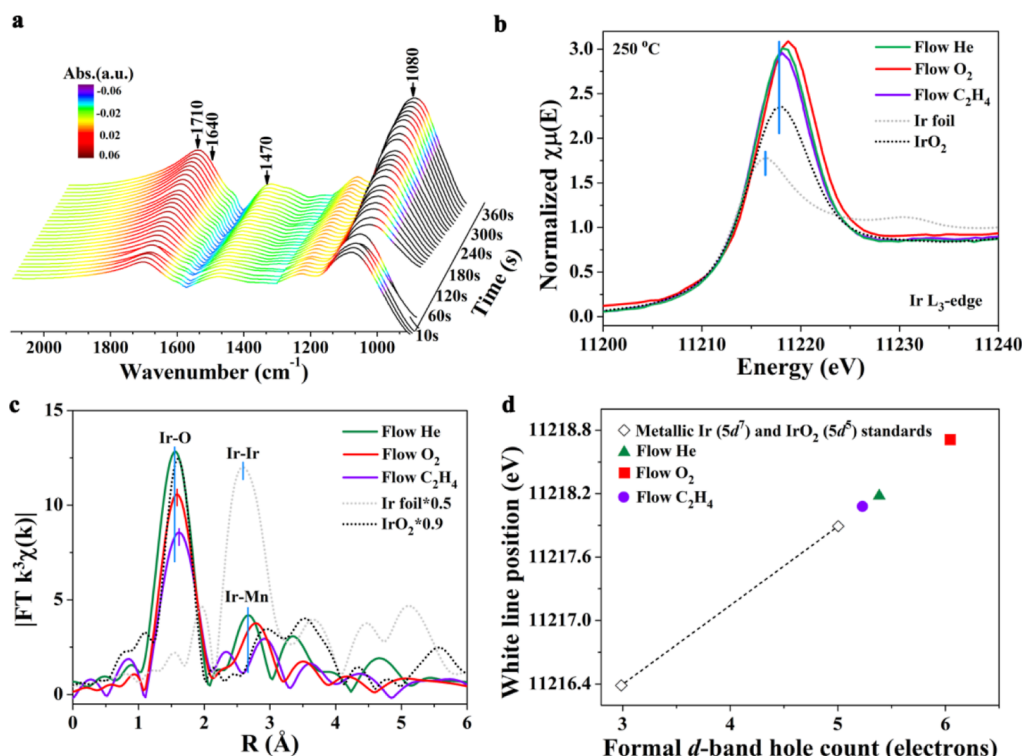


**Figure 4.** (a) *In situ* IR spectra of  $\text{Ir}_1/\alpha\text{-MnO}_2$  under an ethylene/O<sub>2</sub>/He atmosphere at 250 °C. (b) Normalized XANES spectra of  $\text{Ir}_1/\alpha\text{-MnO}_2$  measured under different atmospheres at the iridium L<sub>3</sub>-edge during the reaction process of ethylene epoxidation. (c) EXAFS FT spectra of  $\text{Ir}_1/\alpha\text{-MnO}_2$  under different atmospheres, Ir foil, and  $\text{IrO}_2$ . (d) White-line position of  $\text{Ir}_1/\alpha\text{-MnO}_2$  as a function of the formal d-band hole count. Formal  $\Delta d$  values were calculated based on the white-line shift, and the increase of 0.925 eV per d-band hole was calibrated from metallic iridium ( $5\text{d}^76\text{s}^2$ ) and  $\text{IrO}_2$  ( $5\text{d}^56\text{s}^0$ ) references.

result obtained after exposure of the  $\text{Ir}_1/\alpha\text{-MnO}_2$  surface to ethylene and  $^{18}\text{O}_2$  shows the emergence of  $\text{C}_2\text{H}_4^{18}\text{O}$  ( $m/z = 45$ ), the consumption of the reactant ethylene ( $m/z = 28$ ) and  $^{18}\text{O}_2$  ( $m/z = 36$ ), but with no detection of  $\text{C}_2\text{H}_4^{16}\text{O}$  ( $m/z = 43$ ). This suggested that it is the adsorbed oxygen, rather than the lattice oxygen in  $\alpha\text{-MnO}_2$ , which took part in the reaction of ethylene epoxidation. *In situ* oxygen 1s XPS was conducted for further confirmation. The low-binding-energy peak located at 529.6–529.8 eV can be ascribed to lattice oxygen ( $\text{O}_{\text{lat}}$ ) (Figure S25), and the high-binding-energy peak at 530.9–531.2 eV can be assigned to surface-adsorbed oxygen ( $\text{O}_{\text{ads}}$ ).<sup>67</sup> For  $\text{Ir}_1/\alpha\text{-MnO}_2$ , the percentage of  $\text{O}_{\text{ads}}$  increased after exposure to an oxygen atmosphere, whereas the amount of  $\text{O}_{\text{ads}}$  decreased when the sample was treated with both ethylene and the mixed gas, thus directly indicating that the surface-adsorbed oxygen participated in the epoxidation of ethylene. The O<sub>2</sub> temperature-programmed desorption mass spectrometry (O<sub>2</sub>-TPD-MS) helped to further investigate the adsorbed oxygen species. The peak area of surface-active oxygen species (desorption temperature of 400–600 °C) in  $\text{Ir}_1/\alpha\text{-MnO}_2$  is considerably larger than that of  $\alpha\text{-MnO}_2$  (Figure S26), suggesting that the introduction of iridium increased the amount of the surface-adsorbed oxygen species and thus promoted ethylene epoxidation. Moreover, the oxygen K-edge XANES spectra showed that the absorption peak intensity of  $\text{Ir}_1/\alpha\text{-MnO}_2$  decreased significantly compared with that of  $\alpha\text{-MnO}_2$  (Figure S27), indicating that iridium single atoms induced some change in the electronic structure around oxygen ions but barely any change around the manganese ions, which might result in the increased mobility of active oxygen species after the introduction of iridium. In

addition, the intensity of the absorption peaks for  $\text{Ir}_1/\alpha\text{-MnO}_2$  changed significantly after the epoxidation of ethylene (Figure S27), which further confirmed that the adsorbed active oxygen species was involved in the reaction.

**Mechanistic Study of  $\text{Ir}_1/\alpha\text{-MnO}_2$  for Ethylene Epoxidation.** We conducted *in situ* diffuse reflectance infrared Fourier transform spectroscopy (DRIFTS) to capture the signals of the reaction intermediates on the  $\text{Ir}_1/\alpha\text{-MnO}_2$  surface during ethylene epoxidation. The band at 1470 and 1640 cm<sup>-1</sup> can be indexed to the stretching vibration of ethylene (Figure 4a).<sup>26,56</sup> In addition, two increasing characteristic bands at 1080 and 1710 cm<sup>-1</sup> could be found in the time-resolved DRIFTS spectra in the atmosphere of a mixed gas of ethylene and oxygen. The new band at 1080 cm<sup>-1</sup> can be attributed to the intermediates of O–C–C stretching vibrations in compounds,<sup>56</sup> and the band at 1710 cm<sup>-1</sup> is assigned to C=O stretching vibrations in the compounds.<sup>56,64</sup>

*In situ* XAS was conducted to track the evolution of electronic structures and to identify the real active sites of  $\text{Ir}_1/\alpha\text{-MnO}_2$  during the ethylene epoxidation process. The *in situ* XANES spectra of  $\text{Ir}_1/\alpha\text{-MnO}_2$  were recorded under steady-state conditions with He, O<sub>2</sub>, and ethylene flows at 250 °C, which show pronounced changes in the white-line positions and intensities (Figure 4b). First, a steep typical feature of highly oxidized iridium species was observed. Next, when the atmosphere was switched to ethylene, we found that the white-line position shifted slightly toward lower absorption energies, and the white-line intensity decreased. This behavior is attributed to the bonding of ethylene on the surface of Ir–O species [Ir–O–(π-bonded ethylene)], and the electron transfer from the d-band of iridium to the 2π\* orbital of

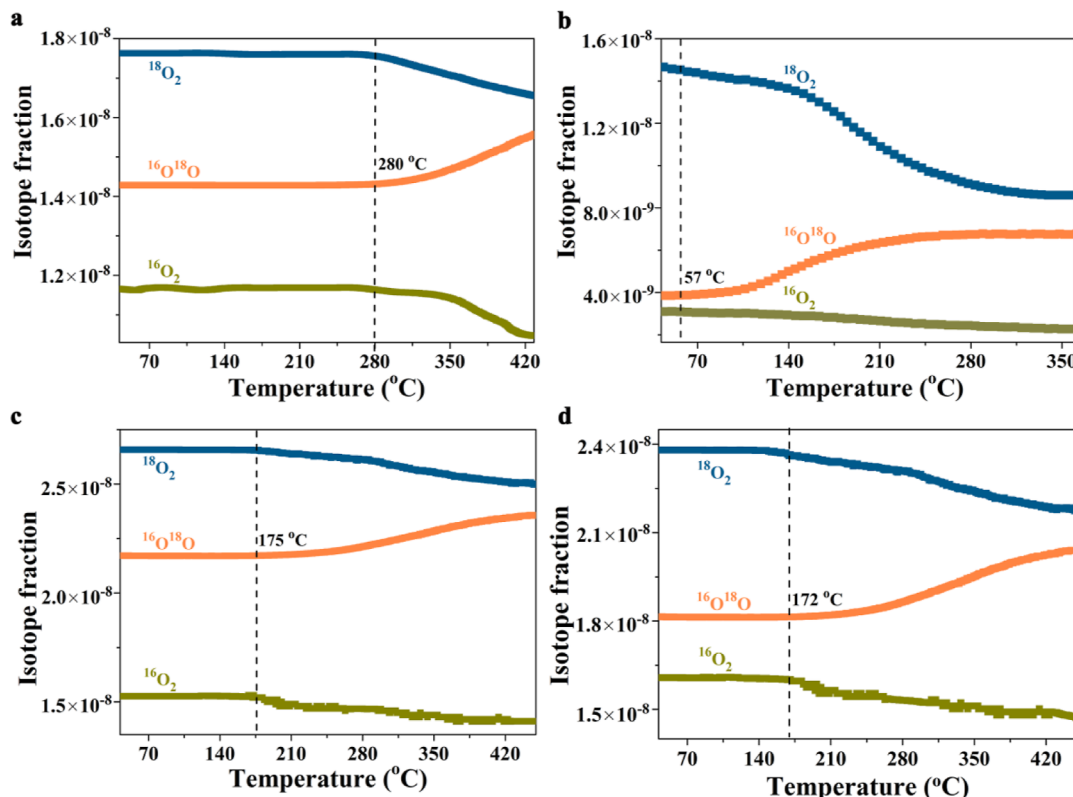


**Figure 5.** Oxygen isotope experiments of (a)  $\text{Ir}_1/\alpha\text{-MnO}_2$  and (c)  $\text{Ag NPs}/\alpha\text{-Al}_2\text{O}_3$  under  $^{16}\text{O}_2/^{18}\text{O}_2/\text{He}$  at different temperatures. Oxygen isotope experiments of (b)  $\text{Ir}_1/\alpha\text{-MnO}_2$  and (d)  $\text{Ag NPs}/\alpha\text{-Al}_2\text{O}_3$  under the mixture of  $^{16}\text{O}_2/^{18}\text{O}_2/\text{He}$  and ethylene/He at different temperatures.

carbon. In addition, as shown in the FT-EXAFS data (Figures 4c and S28–S32; Table S4), when the atmosphere was switched from He to  $\text{O}_2$  and then to ethylene, there was an increase in the Ir–O bond length, indicating that the Ir–O bonds are stretched under realistic operational conditions. The change in bond length for  $\text{Ir}_1/\alpha\text{-MnO}_2$  is mainly attributed to a change in the oxidation state of iridium sites and the local atomic environment at the Ir–O– $\text{MnO}_x$  interface. Figure 4d shows the white-line position of the  $\text{Ir}_1/\alpha\text{-MnO}_2$  catalyst in different atmospheres as a function of the formal *d*-band hole count obtained from iridium ( $5\text{d}^76\text{s}^2$ ) and  $\text{IrO}_2$  ( $5\text{d}^56\text{s}^0$ ) references.<sup>48</sup> Note that the derived slope here is consistent with the value reported in the literature.<sup>65</sup> The absolute numbers of the *d*-band holes in  $\text{Ir}_1/\alpha\text{-MnO}_2$  at He,  $\text{O}_2$ , and ethylene atmospheres are 5.23, 6.05, and 5.36, respectively, which are higher than that of  $\text{IrO}_2$ . In this case, iridium single atoms located at the six-fold manganese site might migrate to the adsorbed site when the atmosphere is switched from  $\text{O}_2$  to ethylene; that is, iridium single atoms on  $\alpha\text{-MnO}_2$  can adjust their locations from the substitutional sites to the adsorbed sites when the atmosphere is changed from oxygen to ethylene. Notably, a total energy shift of 0.62 eV was found over different atmospheres, indicating an  $\text{Ir}^{4+}/\text{Ir}^{5+}$  redox process. In addition,  $\text{Ir NPs}/\alpha\text{-MnO}_2$  shows a similar highly oxidized feature, but its white-line position has no significant shift when the atmosphere was switched from He to  $\text{O}_2$  and then to ethylene (Figure S33). The formal *d*-band hole counts of iridium under different atmospheres were almost identical, implying a similar oxidation state, and the ethylene molecule seems to have no strong interaction with the surface of Ir NPs. The *in situ* XAS results confirmed that, during ethylene epoxidation,  $\text{Ir}_1/\alpha\text{-MnO}_2$  was almost completely oxidized, and

the resulting +4.48 valence state of Ir in the  $\text{Ir}-\text{O}-\text{MnO}_x$  state served as the real active sites, whose 5d band occupancy became higher because of the electron transfer from ethylene to iridium during ethylene epoxidation.

The *in situ* IR results confirmed the  $\pi$  coordination between iridium single atoms and ethylene. The iridium single atom, molecular oxygen, and ethylene collectively constitute a molecular-like catalyst, and this model was simulated *via* theoretical calculations. In order to identify the dissociation ability of molecular oxygen on different catalysts, the gaseous mixture of  $^{16}\text{O}_2$  and  $^{18}\text{O}_2$  was used as a tracer. The catalyst surface can be viewed as a catalyst bed, on which  $^{16}\text{O}_2/^{18}\text{O}_2$  molecules are adsorbed and dissociated into individual oxygen atoms ( $^{16}\text{O}/^{18}\text{O}$ ). The concentrations of  $^{18}\text{O}_2$ ,  $^{16}\text{O}^{18}\text{O}$ , and  $^{16}\text{O}_2$ , corresponding to MS peaks at *m/z* 36, 34, and 32, respectively, provide information about the dissociation of  $^{16}\text{O}_2/^{18}\text{O}_2$  on the catalyst surface. As shown in Figure 5a, no discernible change in the signals of  $^{18}\text{O}_2$ ,  $^{16}\text{O}^{18}\text{O}$ , and  $^{16}\text{O}_2$  at 250 °C was observed, indicating that the dissociation of molecular oxygen is rather difficult on  $\text{Ir}_1/\alpha\text{-MnO}_2$  at this temperature. At 280 °C, the isotope experiment of  $\text{Ir}_1/\alpha\text{-MnO}_2$  shows the dissociation of a considerable portion of introduced  $^{18}\text{O}_2$  and  $^{16}\text{O}_2$ , with the increase of the  $^{16}\text{O}^{18}\text{O}$  signal and the decrease of the signals of  $^{18}\text{O}_2$  and  $^{16}\text{O}_2$ , suggesting that  $\text{Ir}_1/\alpha\text{-MnO}_2$  has a good ability to dissociate molecular oxygen above this temperature.

In order to investigate the effect of ethylene on the dissociation ability of molecular oxygen on catalysts, we designed the following isotope experiments. The inlet gas was a mixture of isotope ( $^{16}\text{O}_2/^{18}\text{O}_2/\text{He}$ ) and ethylene ( $\text{C}_2\text{H}_4/\text{He}$ ). Surprisingly, for  $\text{Ir}_1/\alpha\text{-MnO}_2$ , the fragment ions of  $^{16}\text{O}^{18}\text{O}$  began to show up at 57 °C (Figure 5b), indicating that the

activation and dissociation ability of molecular oxygen on  $\text{Ir}_1/\alpha\text{-MnO}_2$  was greatly boosted when ethylene was introduced, and the catalytic reaction could be started at this temperature. This was consistent with the catalytic activity results that the onset temperature of the reaction was about 57 °C (Figure 2a). By contrast, for the Ag NPs/ $\alpha\text{-Al}_2\text{O}_3$  catalyst (Figure 5c), the signals for  $^{18}\text{O}_2$ ,  $^{16}\text{O}^{18}\text{O}$ , and  $^{16}\text{O}_2$  changed at 175 °C, suggesting that there were  $^{16}\text{O}_2/^{18}\text{O}_2$  consumed and  $^{16}\text{O}^{18}\text{O}$  produced during the isotope experiment. This onset temperature for  $\text{O}_2$  dissociation was much lower than that on  $\text{Ir}_1/\alpha\text{-MnO}_2$ , indicating that molecular oxygen can be easily dissociated into atomic oxygen on Ag NPs/ $\alpha\text{-Al}_2\text{O}_3$ . Similar trends were observed for Ag NPs/ $\alpha\text{-Al}_2\text{O}_3$  when ethylene was introduced into the system (Figure 5d), implying that ethylene has a negligible effect on the dissociation ability of molecular oxygen on Ag NPs/ $\alpha\text{-Al}_2\text{O}_3$ . Based on the above isotope experiments results, it can be concluded that molecular oxygen was directly involved in the reaction of ethylene epoxidation over  $\text{Ir}_1/\alpha\text{-MnO}_2$ , for which its reaction mechanism was distinct from that of the conventional silver-based catalyst (where atomic oxygen participates in the reaction).

Compared with iridium-free  $\alpha\text{-MnO}_2$  nanorods,  $\text{Ir}_1/\alpha\text{-MnO}_2$  exhibited superior activity and selectivity for ethylene epoxidation. DFT calculations were further performed to unveil the underlying mechanism for the excellent catalytic performance of  $\text{Ir}_1/\alpha\text{-MnO}_2$  nanorods. As shown in the STEM and STEM image simulation results, the iridium single atoms exist in two ways: by being adsorbed on the surface (that is, at the interstitial sites, denoted as “adsorbed  $\text{Ir}_1/\alpha\text{-MnO}_2$ ”) and by substituting manganese atoms (denoted as “substitutional  $\text{Ir}_1/\alpha\text{-MnO}_2$ ”). Hence, both structure configurations were taken into consideration as the initial state for calculating ethylene epoxidation pathways. The O-terminated (110) surface of  $\alpha\text{-MnO}_2$  was selected for the simulation model (Figure S34). The detailed structure of the calculation model of adsorbed  $\text{Ir}_1/\alpha\text{-MnO}_2$  is shown in Figure S35. Based on the experimental results of *in situ* XPS, *in situ* IR, and isotope experiments, it can be inferred that the iridium single atom interacts with ethylene and molecular oxygen in the form of  $\pi$ -coordination instead of the conventional  $\sigma$ -coordination. For the adsorbed  $\text{Ir}_1/\alpha\text{-MnO}_2$ , the first step involves the adsorption of molecular oxygen and ethylene on the iridium single-atom site *via*  $\pi$ -coordination, and the introduction of ethylene facilitates the dissociation of molecular oxygen into atomic oxygen, which directly reacts with an ethylene molecule to produce an EO molecule, with an activation energy of 0.39 eV. In the second step, the other atomic oxygen remaining on the iridium site reacts with another adsorbed ethylene molecule and readily produces a five-membered oxametallacycle intermediate with an activation energy of merely 0.34 eV, eventually yielding another EO molecule (Figure 6a). This five-membered oxametallacycle intermediate has been validated *via* *in situ* IR spectroscopy. During the entire reaction process, the  $\pi$ -coordination structure between iridium and ethylene or molecular oxygen facilitates the formation of five-membered oxametallacycle intermediates, thereby producing EO in a unique manner. Furthermore, the ethylene molecule stretches the Ir–O bond of the outermost layer of oxygen, which is consistent with the EXAFS results. Meanwhile, the adsorbed oxygen is shifted toward ethylene and bonds to ethylene. The interaction between adsorbed oxygen and iridium is reduced, as indicated by theoretical optimization results, and iridium is drawn by the lattice oxygen of  $\alpha\text{-MnO}_2$ .

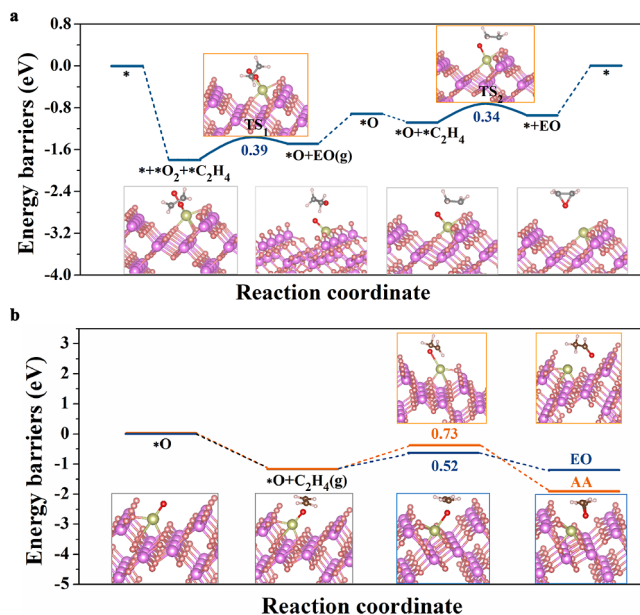


**Figure 6.** Calculated free energy profiles for the epoxidation of ethylene on adsorbed  $\text{Ir}_1/\alpha\text{-MnO}_2$  following (a) our proposed mechanism based on the  $\pi$ -coordination structure between iridium and ethylene or molecular oxygen and the (b) conventional E–R mechanism.

These are conducive to the formation of the five-membered oxametallacycle intermediates and the desired product EO.

In contrast, the reaction pathway is different and much more difficult if it follows the conventional Eley–Rideal (E–R) pathway (Figure 6b). For the adsorbed  $\text{Ir}_1/\alpha\text{-MnO}_2$ , the first step involves the adsorption of an oxygen atom on the iridium single-atom site; the energy barrier for the dissociation of molecular oxygen into atomic oxygen is 0.82 eV. In the second step, the adsorbed oxygen reacts with the gaseous ethylene molecule, directly forming EO with an activation barrier of 0.52 eV. Note that the formed EO on the catalyst surface may rearrange into the byproduct acetaldehyde (AA) with an energy barrier of 0.73 eV. According to our experimental results, the main product of the reaction was EO, and AA was barely detected. It indicates that the ethylene epoxidation reaction catalyzed by the adsorbed  $\text{Ir}_1/\alpha\text{-MnO}_2$  catalyst does not follow this traditional E–R mechanism. Furthermore, the reaction energy barriers of ethylene oxidation over Ag (110) were also calculated for comparison,<sup>49</sup> of which the adsorption energy of oxygen was 1.77 eV, indicating that the epoxidation of ethylene on Ag (110) is rather difficult. The relevant adsorption energies and activation energies are listed in Tables S5 and S6.

In addition, for the substitutional  $\text{Ir}_1/\alpha\text{-MnO}_2$  catalyst (Figure S36), the iridium atom is first saturated by an oxygen atom, which derives from the dissociation of molecular oxygen on the iridium single-atom site, with a dissociation energy barrier of 0.86 eV. The gas-phase ethylene species reacts with the adsorbed oxygen atom to form the ethyoxyl intermediate, and this step proceeds easily, with an energy barrier of 0.35 eV. Subsequently, the isomerization of the ethyoxyl intermediate to EO and acetaldehyde (AA) is rather difficult, for which the reaction barriers are as high as 1.47 and 1.56 eV, respectively. Hence, the substitutional structure of the iridium atom is not as catalytically active for the epoxidation of ethylene. Besides, it is rather difficult to selectively obtain the desired product EO

on the substitutional  $\text{Ir}_1/\alpha\text{-MnO}_2$  owing to its high desorption energy of EO ( $-1.22$  eV). This indicates that in ethylene epoxidation, the catalytically active sites for iridium SAC on  $\alpha\text{-MnO}_2$  are the adsorbed Ir atoms, rather than the substitutional ones. Both the experimental and theoretical analyses validate that during the reaction of ethylene epoxidation, iridium atoms would tend to migrate from the less active substitutional sites toward the more active adsorbed sites. Moreover, the energy barriers of the ethylene epoxidation on pure  $\alpha\text{-MnO}_2$ ,  $\text{IrO}_2$  and Ir NPs/ $\alpha\text{-MnO}_2$  (Figures S37–S39) are higher than that on adsorbed  $\text{Ir}_1/\alpha\text{-MnO}_2$ , confirming the unique advantages of  $\pi$ -coordination between the iridium metal center with a higher oxidation state and ethylene and molecular oxygen and  $\text{Ir}-\text{O}-\text{MnO}_x$  for the catalytic activation of ethylene.

Structural analysis and mechanistic studies demonstrate that the  $\text{Ir}-\text{O}-\text{MnO}_x$  unit of  $\text{Ir}_1/\alpha\text{-MnO}_2$  is the active center for ethylene epoxidation, and the heterogeneous iridium SAC interacts with ethylene and molecular oxygen, resulting in a molecular-like catalyst, eventually achieving the molecular-like catalysis for ethylene epoxidation. Yet still, apart from the iridium single-atom sites, the support itself may also contribute to the overall activity. To clarify the role of  $\alpha\text{-MnO}_2$ , we further synthesized comparison samples of carbon nitride (CN)-supported Ir SAC ( $\text{Ir}_1/\text{CN}$ ),<sup>68</sup>  $\text{Ir}_1/\text{CeO}_2$ ,  $\text{Ir}_1/\text{CeZrO}_x$ ,  $\text{Ir}_1/\text{SiO}_2$ ,  $\text{Ir}_1/\text{Al}_2\text{O}_3$ , and  $\text{Ir}_1/\text{ZSM-5}$  catalysts (with the same iridium loading) and tested their ethylene epoxidation performances. The results indicated that although  $\text{Ir}_1/\text{CN}$ ,  $\text{Ir}_1/\text{CeO}_2$ ,  $\text{Ir}_1/\text{CeZrO}_x$ ,  $\text{Ir}_1/\text{SiO}_2$ ,  $\text{Ir}_1/\text{Al}_2\text{O}_3$ , and  $\text{Ir}_1/\text{ZSM-5}$  have similar iridium single-atom sites, they exhibited low activities (<25%) and EO selectivities (<16%) for ethylene epoxidation (Figure S40). Both  $\text{Ir}_1/\text{CeO}_2$  and  $\text{Ir}_1/\text{Al}_2\text{O}_3$  exhibited di- $\sigma$ -bonded ethylene adsorption mode (Figure S41). This confirms that the unique  $\pi$ -coordination structure between ethylene and iridium single atoms, the  $\text{Ir}-\text{O}-\text{MnO}_x$  unit on the  $\alpha\text{-MnO}_2$  support, and the flexible redox ability (Figure S42) of  $\alpha\text{-MnO}_2$  are the indispensable factors that contribute to the outstanding ethylene epoxidation performance of  $\text{Ir}_1/\alpha\text{-MnO}_2$ .

## CONCLUSIONS

In summary, we have developed a new catalytic strategy for ethylene epoxidation, namely, the heterogeneous iridium single atoms anchored on  $\alpha\text{-MnO}_2$  nanorods ( $\text{Ir}_1/\alpha\text{-MnO}_2$ ) to interact with ethylene and molecular oxygen, resulting in a molecular-like catalyst, whose catalytic properties were close to those in molecular catalysis and distinct from that of iridium nanoparticle counterparts.  $\text{Ir}_1/\alpha\text{-MnO}_2$  exhibited a remarkable activity for ethylene epoxidation, 7.6 times higher than that of Ag NPs/ $\alpha\text{-Al}_2\text{O}_3$ , with a near-unity selectivity (~99%) for the desired product EO. *In situ* experiments and quantum-chemistry calculations indicated that the  $\pi$ -coordination structure between Ir, ethylene, and molecular oxygen can promote the formation of five-membered oxametallacycle intermediates and accelerate the formation of EO, and this reaction mechanism is different from the conventional E–R mechanism of silver-based catalysts. Our work here offers an in-depth understanding of the local structure of single atoms on oxide supports under realistic catalytic conditions, and this exquisite catalytic strategy can be used to regulate the oxidation performance of metals. Implementing the concepts of homogeneous catalysis into the gas–solid phase catalytic reactions would provide new perspectives for the design of new advanced catalysts.

## ASSOCIATED CONTENT

### SI Supporting Information

The Supporting Information is available free of charge at <https://pubs.acs.org/doi/10.1021/jacs.2c11380>.

Additional experimental details, materials, and methods, including photographs of the experimental setup (PDF)

## AUTHOR INFORMATION

### Corresponding Authors

Xin Chen – Beijing Advanced Innovation Center for Materials Genome Engineering, Institute of Solid State Chemistry, University of Science and Technology Beijing, Beijing 100083, China; Email: [chenx@ustb.edu.cn](mailto:chenx@ustb.edu.cn)

Chen Chen – Engineering Research Center of Advanced Rare Earth Materials, Department of Chemistry, Tsinghua University, Beijing 100084, China;  [orcid.org/0000-0001-5902-3037](https://orcid.org/0000-0001-5902-3037); Email: [cchen@mail.tsinghua.edu.cn](mailto:cchen@mail.tsinghua.edu.cn)

### Authors

Hongling Yang – Engineering Research Center of Advanced Rare Earth Materials, Department of Chemistry, Tsinghua University, Beijing 100084, China; Beijing Key Laboratory for VOCs Pollution Prevention and Treatment Technology and Application of Urban Air, Beijing Municipal Research Institute of Eco-Environmental Protection, Beijing 100037, China

Xiaoxu Wang – DP Technology, Beijing 100080, China

Qinggang Liu – Engineering Research Center of Advanced Rare Earth Materials, Department of Chemistry, Tsinghua University, Beijing 100084, China

Aijian Huang – Engineering Research Center of Advanced Rare Earth Materials, Department of Chemistry, Tsinghua University, Beijing 100084, China;  [orcid.org/0000-0002-3483-3233](https://orcid.org/0000-0002-3483-3233)

Xun Zhang – School of Physical Science and Technology, Shanghai Tech University, Shanghai 201210, China

Yi Yu – School of Physical Science and Technology, Shanghai Tech University, Shanghai 201210, China;  [orcid.org/0000-0003-4326-5992](https://orcid.org/0000-0003-4326-5992)

Zewen Zhuang – Engineering Research Center of Advanced Rare Earth Materials, Department of Chemistry, Tsinghua University, Beijing 100084, China; College of Materials Science and Engineering, Fuzhou University, Fuzhou 350108, China;  [orcid.org/0000-0002-7060-426X](https://orcid.org/0000-0002-7060-426X)

Ganggang Li – National Engineering Laboratory for VOCs Pollution Control Material & Technology, Research Center for Environmental Material and Pollution Control Technology, University of Chinese Academy of Sciences, Beijing 101408, China;  [orcid.org/0000-0003-2657-3694](https://orcid.org/0000-0003-2657-3694)

Yang Li – Beijing Single-Atom Catalysis Technology Co., Ltd., Beijing 100094, China

Qing Peng – Engineering Research Center of Advanced Rare Earth Materials, Department of Chemistry, Tsinghua University, Beijing 100084, China

Hai Xiao – Engineering Research Center of Advanced Rare Earth Materials, Department of Chemistry, Tsinghua University, Beijing 100084, China;  [orcid.org/0000-0001-9399-1584](https://orcid.org/0000-0001-9399-1584)

Complete contact information is available at:

<https://pubs.acs.org/10.1021/jacs.2c11380>

**Author Contributions**

○ H.Y. and X.W. contributed equally.

**Funding**

This work was supported by the National Natural Science Foundation of China (21925202, 22202014, 22008006, and U22B2071), National Key R&D Program of China (2021YFF0500503), Fund Project of Beijing Municipal Research Institute of Eco-Environmental Protection (Y2023-005), National Environmental Protection Standard Project (JZ2022-012), Young Elite Scientists Sponsorship Program by BAST, and Fundamental Research Funds for the Central Universities (FRF-IDRY-20-005 and FRF-TP-20-077A1).

**Notes**

The authors declare no competing financial interest.

**ACKNOWLEDGMENTS**

We thank the Tsinghua National Laboratory for Information Science and Technology and USTB MatCom of Beijing Advanced Innovation Center for Materials Genome Engineering for providing grid resources that have contributed to the calculation results. We acknowledge the support of the Analysis Center of Tsinghua University for XPS measurements. We thank the BL11B station at the Shanghai Synchrotron Radiation Facility and the 1W1B and 4B7A stations at the Beijing Synchrotron Radiation Facility. We thank the Bohrium Cloud Platform (<https://bohrium.dp.tech>) of DP Technology for computing support. We thank the support of the Institute of Physics, Chinese Academy of Sciences for HAADF-STEM measurements. Also, we thank Dr. C. Zhang for helping in preparing this article.

**REFERENCES**

- (1) Witham, C. A.; et al. Converting homogeneous to heterogeneous in electrophilic catalysis using monodisperse metal nanoparticles. *Nat. Chem.* **2010**, *2*, 36–41.
- (2) Cui, X. J.; et al. Bridging homogeneous and heterogeneous catalysis by heterogeneous single-metal-site catalysts. *Nat. Catal.* **2018**, *1*, 385–397.
- (3) Samantaray, M. K.; et al. The comparison between single atom catalysis and surface organometallic catalysis. *Chem. Rev.* **2020**, *120*, 734–813.
- (4) Huang, Y. B.; et al. Soluble metal-nanoparticle-decorated porous coordination polymers for the homogenization of heterogeneous catalysis. *J. Am. Chem. Soc.* **2016**, *138*, 10104.
- (5) Shylesh, S.; et al. Magnetically separable nanocatalysts: bridges between homogeneous and heterogeneous catalysis. *Angew. Chem., Int. Ed.* **2010**, *49*, 3428–3459.
- (6) Gross, E.; et al. Polymer-encapsulated metallic nanoparticles as a bridge between homogeneous and heterogeneous catalysis. *Catal. Lett.* **2015**, *145*, 126–138.
- (7) Yang, X. F.; et al. Single-atom catalysts: a new frontier in heterogeneous catalysis. *Acc. Chem. Res.* **2013**, *46*, 1740–1748.
- (8) McMorn, P.; et al. Heterogeneous enantioselective catalysts: strategies for the immobilisation of homogeneous catalysts. *Chem. Soc. Rev.* **2004**, *33*, 108–122.
- (9) Garrido-Barros, P.; et al. Electronic  $\pi$ -delocalization boosts catalytic water oxidation by Cu (II) molecular catalysts heterogenized on graphene sheets. *J. Am. Chem. Soc.* **2017**, *139*, 12907–12910.
- (10) Chen, C.; et al. Highly crystalline multimetallic nanoframes with three-dimensional electrocatalytic surfaces. *Science* **2014**, *343*, 1339–1343.
- (11) Zhuang, Z. B.; et al. Controlled synthesis of semiconductor nanostructures in the liquid phase. *Chem. Soc. Rev.* **2011**, *40*, 5492–5513.
- (12) Wu, Y. E.; et al. Syntheses of water-soluble octahedral, truncated octahedral, and cubic Pt-Ni nanocrystals and their structure-activity study in model hydrogenation reactions. *J. Am. Chem. Soc.* **2012**, *134*, 8975–8981.
- (13) Kim, S. M.; et al. Postsynthetic functionalization of a hollow silica nanoreactor with manganese oxide-immobilized metal nanocrystals inside the cavity. *J. Am. Chem. Soc.* **2013**, *135*, 15714–15717.
- (14) Thomas, J. M.; et al. Tens of thousands of atoms replaced by one. *Nature* **2015**, *525*, 325–326.
- (15) Jones, J.; et al. Thermally stable single-atom platinum-on-ceria catalysts via atom trapping. *Science* **2016**, *353*, 150–154.
- (16) Qiao, B. T.; et al. Single-atom catalysis of CO oxidation using Pt<sub>1</sub>/FeO<sub>x</sub>. *Nat. Chem.* **2011**, *3*, 634–641.
- (17) Yang, H. L.; et al. Factors affecting the catalytic performance of nano-catalysts. *Chin. J. Chem.* **2022**, *40*, 515–523.
- (18) Zhao, Z. K.; et al. Cobalt-modified molybdenum carbide as an efficient catalyst for chemoselective reduction of aromatic nitro compounds. *Green Chem.* **2014**, *16*, 1274–1281.
- (19) Yang, H. L.; et al. Manganese vacancy-confined single-atom Ag in cryptomelane nanorods for efficient Wacker oxidation of styrene derivatives. *Chem. Sci.* **2021**, *12*, 6099–6106.
- (20) Choi, C. H.; et al. Tuning selectivity of electrochemical reactions by atomically dispersed platinum catalyst. *Nat. Commun.* **2016**, *7*, 10922–10930.
- (21) Yang, H. L.; et al. Isolated single-atom Ruthenium anchored on Beta zeolite as an efficient heterogeneous catalyst for styrene epoxidation. *ChemNanoMat* **2020**, *6*, 1647–1651.
- (22) Schilter, D.; et al. Oxidation reactions: a chameleon catalyst. *Nat. Rev. Chem.* **2017**, *1*, 0050.
- (23) Zheng, Z. T.; et al. Homogeneous gold-catalyzed oxidation reactions. *Chem. Rev.* **2021**, *121*, 8979–9038.
- (24) Pu, T. C.; et al. Overview of selective oxidation of ethylene to ethylene oxide by Ag catalysts. *ACS Catal.* **2019**, *9*, 10727–10750.
- (25) Leow, W. R.; et al. Chloride-mediated selective electrosynthesis of ethylene and propylene oxides at high current density. *Science* **2020**, *368*, 1228–1233.
- (26) Yang, H. L.; et al. Fluorine-enhanced Pt/ZSM-5 catalysts for low temperature oxidation of ethylene. *Catal. Sci. Technol.* **2018**, *8*, 1988–1996.
- (27) van Hoof, A. J. F.; et al. Structure sensitivity of silver-catalyzed ethylene epoxidation. *ACS Catal.* **2019**, *9*, 9829–9839.
- (28) Yang, H. L.; et al. Understanding the active sites of Ag/zeolites and deactivation mechanism of ethylene catalytic oxidation at room temperature. *ACS Catal.* **2018**, *8*, 1248–1258.
- (29) Yang, H. L.; et al. Synthesis, characterization and evaluations of the Ag/ZSM-5 for ethylene oxidation at room temperature: Investigating the effect of water and deactivation. *Chem. Eng. J.* **2018**, *347*, 808–818.
- (30) Özbek, M. O.; et al. Chlorine and caesium promotion of silver ethylene epoxidation catalysts. *ChemCatChem* **2013**, *5*, 443–451.
- (31) Ren, D. M.; et al. Origin of enhanced ethylene oxide selectivity by Cs-promoted silver catalyst. *Mol. Catal.* **2017**, *441*, 92–99.
- (32) Diao, W. J.; et al. An investigation on the role of Re as a promoter in Ag-Cs-Re/ $\alpha$ -Al<sub>2</sub>O<sub>3</sub> high-selectivity, ethylene epoxidation catalysts. *J. Catal.* **2015**, *322*, 14–23.
- (33) Salaev, M. A.; et al. Towards the understanding of promoting effects of Re, Cs and Cl promoters for silver catalysts of ethylene epoxidation: a computational study. *Catal. Today* **2021**, *375*, 585–590.
- (34) Campbell, C. T.; et al. Chlorine promotion of selective ethylene oxidation over Ag (110): kinetics and mechanism. *J. Catal.* **1985**, *92*, 272–283.
- (35) Tan, S. A.; et al. Chlorine-oxygen interactions and the role of chlorine in ethylene oxidation over Ag (111). *J. Catal.* **1986**, *100*, 383–391.
- (36) Ramirez, A.; et al. A nanoarchitecture based on silver and copper oxide with an exceptional response in the chlorine-promoted epoxidation of ethylene. *Angew. Chem., Int. Ed.* **2016**, *55*, 11158–11161.

- (37) Greiner, M.; et al. Phase coexistence of multiple copper oxides on AgCu catalysts during ethylene epoxidation. *ACS Catal.* **2018**, *8*, 2286–2295.
- (38) Li, Z. H.; et al. Enhanced ethylene oxide selectivity by Cu and Re dual-promoted Ag catalysts. *Ind. Eng. Chem. Res.* **2018**, *57*, 4180–4185.
- (39) Rojuechai, S.; et al. Catalytic activity of ethylene oxidation over Au, Ag and Au-Ag catalysts: Support effect. *Catal. Commun.* **2007**, *8*, 57–64.
- (40) Linic, S.; et al. Formation of a stable surface oxametallacycle that produces ethylene oxide. *J. Am. Chem. Soc.* **2002**, *124*, 310–317.
- (41) Linic, S.; et al. Ethylene epoxidation on Ag: identification of the crucial surface intermediate by experimental and theoretical investigation of its electronic structure. *Angew. Chem., Int. Ed.* **2004**, *43*, 2918–2921.
- (42) Nájera, C.; et al. Metal-catalyzed regiodivergent organic reactions. *Chem. Soc. Rev.* **2019**, *48*, 4515–4618.
- (43) Valero, M.; et al. NHC-stabilized iridium nanoparticles as catalysts in hydrogen isotope exchange reactions of anilines. *Angew. Chem., Int. Ed.* **2020**, *59*, 3517–3522.
- (44) Linares, M.; et al. Valence bond approach of metal-ligand bonding in the Dewar-Chatt-Duncanson model. *Inorg. Chem.* **2007**, *46*, 11390–11396.
- (45) Perdew, J. P.; et al. Generalized gradient approximation made simple. *Phys. Rev. Lett.* **1996**, *77*, 3865–3868.
- (46) Henkelman, G.; et al. A climbing image nudged elastic band method for finding saddle points and minimum energy paths. *J. Chem. Phys.* **2000**, *113*, 9901–9904.
- (47) Chen, X.; et al. Characterization of manganese oxide octahedral molecular sieve (M-OMS-2) materials with different metal cation dopants. *Chem. Mater.* **2002**, *14*, 940–948.
- (48) Nong, H. N.; et al. A unique oxygen ligand environment facilitates water oxidation in hole-doped  $\text{IrNiO}_x$  core-shell electrocatalysts. *Nat. Catal.* **2018**, *1*, 841–851.
- (49) Christopher, P.; et al. Engineering selectivity in heterogeneous catalysis: Ag nanowires as selective ethylene epoxidation catalysts. *J. Am. Chem. Soc.* **2008**, *130*, 11264–11265.
- (50) Chen, C. J.; et al. Kinetics of ethylene epoxidation on a promoted Ag/ $\alpha$ -Al<sub>2</sub>O<sub>3</sub> catalyst—the effects of product and chloride co-feeding on rates and selectivity. *Chem. - Eur. J.* **2018**, *24*, 12405–12415.
- (51) Lafarga, D.; et al. Ethylene epoxidation on Ag-Cs/ $\alpha$ -Al<sub>2</sub>O<sub>3</sub> catalyst: experimental results and strategy for kinetic parameter determination. *Ind. Eng. Chem. Res.* **2000**, *39*, 2148–2156.
- (52) Park, D. W.; et al. Ethylene epoxidation on a silver catalyst: unsteady and steady state kinetics. *J. Catal.* **1987**, *105*, 81–94.
- (53) Klugherz, P. D.; et al. Kinetics of ethylene oxidation on a supported silver catalyst. *AIChE J.* **1971**, *17*, 856–866.
- (54) Nault, L. G.; et al. Reaction studies of catalytic rate studies of catalytic oxidation of ethylene. *Ind. Eng. Chem. Process Des. Dev.* **1962**, *1*, 285–292.
- (55) Chen, N.; et al. Porous carbon nanowire array for surface-enhanced Raman spectroscopy. *Nat. Commun.* **2020**, *11*, 4772–4779.
- (56) Force, E. L.; et al. Infrared spectra of adsorbed species present during the oxidation of ethylene over silver. *J. Catal.* **1975**, *38*, 440–460.
- (57) Yin, J.; et al. Site switching from di- $\sigma$  ethylene to  $\pi$ -bonded ethylene in the presence of coadsorbed nitrogen on Pt (111). *J. Phys. Chem. C* **2010**, *114*, 12230–12233.
- (58) Bent, B. E.; et al. Molecular ethylene Adsorption on Rh (111) and Rh (100): estimation of the C-C stretching force constant from the surface vibrational frequencies. *J. Phys. Chem.* **1988**, *92*, 4720–4726.
- (59) Argo, A. M.; Odzak, J. F.; Lai, F. S.; Gates, B. C. Observation of ligand effects during alkene hydrogenation catalysed by supported metal clusters. *Nature* **2002**, *415*, 623–626.
- (60) Gao, H. J.; et al. A first-principles study of oxygen adsorption on Ir(111) surface. *Appl. Surf. Sci.* **2016**, *389*, 211–215.
- (61) Maintz, S.; et al. Analytic projection from plane-wave and PAW wavefunctions and application to chemical-bonding analysis in solids. *J. Compu. Chem.* **2013**, *34*, 2557–2567.
- (62) Yang, L. M.; et al. Two-dimensional Cu<sub>2</sub>Si monolayer with planar hexacoordinate copper and silicon bonding. *J. Am. Chem. Soc.* **2015**, *137*, 2757–2762.
- (63) Zhao, D.; et al. MXene (Ti<sub>3</sub>C<sub>2</sub>) vacancy-confined single-atom catalyst for efficient functionalization of CO<sub>2</sub>. *J. Am. Chem. Soc.* **2019**, *141*, 4086–4093.
- (64) Maintz, S.; et al. LOBSTER: a tool to extract chemical bonding from plane-wave based DFT. *J. Compu. Chem.* **2016**, *37*, 1030–1035.
- (65) Galeev, T. R.; et al. Solid state adaptive natural density partitioning: a tool for deciphering multi-center bonding in periodic systems. *Phys. Chem. Chem. Phys.* **2013**, *15*, 5022–54029.
- (66) Mihaylov, M.; et al. New types of nonclassical Iridium carbonyls formed in Ir-ZSM-5: a Fourier transform Infrared spectroscopy investigation. *J. Phys. Chem. B* **2006**, *110*, 10383–10389.
- (67) Zhang, M.; et al. Effects of the surface adsorbed oxygen species tuned by rare-earth metal doping on dry reforming of methane over Ni/ZrO<sub>2</sub> catalyst. *Appl. Catal. B: Environ.* **2020**, *264*, 118522–118533.
- (68) Li, Z.; et al. Iridium single-atom catalyst on nitrogen-doped carbon for formic acid oxidation synthesized using a general host-guest strategy. *Nat. Chem.* **2020**, *12*, 764–772.

## □ Recommended by ACS

### Circumventing CO<sub>2</sub> Reduction Scaling Relations Over the Heteronuclear Diatomic Catalytic Pair

Jie Ding, Bin Liu, et al.

MAY 18, 2023

JOURNAL OF THE AMERICAN CHEMICAL SOCIETY

READ ▶

### Modulating Charges of Dual Sites in Multivariate Metal–Organic Frameworks for Boosting Selective Aerobic Epoxidation of Alkenes

Hanlin Liu, Guodong Li, et al.

MAY 10, 2023

JOURNAL OF THE AMERICAN CHEMICAL SOCIETY

READ ▶

### Generation of Pd–O for Promoting Electrochemical H<sub>2</sub>O<sub>2</sub> Production

Jiawei Du, Yijin Kang, et al.

MAY 05, 2023

ACS CATALYSIS

READ ▶

### General Synthesis of a Diatomic Catalyst Library via a Macrocyclic Precursor-Mediated Approach

Yu-Xiao Zhang, Zhiqiang Niu, et al.

FEBRUARY 15, 2023

JOURNAL OF THE AMERICAN CHEMICAL SOCIETY

READ ▶

Get More Suggestions >